



ZnO_{1-x}/carbon dots composite hollow spheres: Facile aerosol synthesis and superior CO₂ photoreduction under UV, visible and near-infrared irradiation

Liang-Yi Lin^a, Shaline Kavadiya^a, Bedia Begum Karakocak^a, Yao Nie^a, Ramesh Raliya^a, Steven T. Wang^b, Mikhail Y. Berezin^b, Pratim Biswas^{a,*}

^a Aerosol and Air Quality Research Laboratory, Center for Aerosol Science and Engineering, Department of Energy, Environmental and Chemical Engineering, Washington University in St. Louis, St. Louis, MO 63130, USA

^b Department of Radiology, Washington University in St. Louis School of Medicine, St. Louis, MO 63110, USA

ARTICLE INFO

Keywords:

Photocatalysis
Hollow spheres
Carbon dots
Oxygen-deficient ZnO
CO₂
Reduction

ABSTRACT

For the first time, ZnO_{1-x}/carbon dots composite hollow spheres (denoted ZnO_{1-x}/C) have been synthesized via a single-step aerosol process and employed for CO₂ photoreduction over the whole UV–vis–NIR spectrum. The effects of the precursor component ratio and synthesis temperature on the physicochemical properties of the composites are systematically investigated to maximize CO₂ conversion efficiency. Under UV–vis–NIR light, the best performing sample had an average CO production rate of 60.77 μmol g⁻¹ h⁻¹, which is about 54.7 times higher than that of pristine ZnO, and 11.5 times higher than that of commercial TiO₂ (Degussa-P25). More importantly, whereas ZnO and Degussa-P25 are photocatalytically inactive, the photocatalytic response of the ZnO_{1-x}/C composite was successfully achieved under NIR illumination alone, with an average CO production rate of 15.98 μmol g⁻¹ h⁻¹. The realization of NIR-driven CO₂ photoreduction with enhanced photocatalytic activity benefits from 1) the hollow structure, which allows multiple internal reflections of light for enhanced light absorption; 2) the oxygen deficiency of ZnO_{1-x} and the deposited carbon, which enable efficient charge carrier transfer and improved CO₂ adsorption; and 3) the strong NIR absorption of ZnO_{1-x}/C, in which ZnO_{1-x} is excited by absorbing the up-converted photoluminescence emissions (410–560 nm) of the carbon dots.

1. Introduction

Photocatalytic reduction of CO₂ by H₂O vapor to produce value-added fuels (e.g., CO and CH₄) is also one of the most promising technologies to mitigate CO₂ [1]. To date, various nanostructured photocatalysts, such as TiO₂, ZnO, CdS, and WO₃, have been demonstrated for CO₂ photoreduction [2–5]. Nevertheless, most of these photocatalysts are active only under ultraviolet (UV) and/or visible (Vis) light, which respectively constitute only ~4% and 46% of the solar spectrum [6,7]. Owing to the difficulties in harnessing low-photon-energy NIR light to reduce highly stable CO₂ molecules, so far, there are only a few reports on the photoreduction of CO₂ using near-infrared (NIR) light [8,9], which accounts for ~50% of the solar spectrum. Consequently, a photocatalyst that can effectively utilize the full solar spectrum is highly desirable.

As a potential photocatalyst, ZnO has remarkable properties, such as nontoxicity, thermal/mechanical stability, high photosensitivity, and high redox potential [10]. Nevertheless, for practical uses, ZnO has insufficient catalytic efficiency, which mainly originates from the fast

recombination of photogenerated electron-hole (e⁻-h⁺) pairs [11]. Moreover, its wide band gap (~3.2 eV) makes it active only in the UV region, so it does not utilize most of the solar spectrum [12]. To overcome these limitations, semiconductor photocatalysts (e.g., TiO₂ and ZnO) were engineered by introducing oxygen vacancies to tailor the band energy levels and effectively extend the light absorption in the visible region [13–15]. The formation of additional oxygen vacancy energy bands, acting as donor states, between the conduction band (CB) and valence band (VB) of the semiconductors, promotes the sub-bands' excitation of electrons by absorption of visible light [14]. However, there has been no report yet on NIR-driven photocatalysis using oxygen-deficient ZnO materials.

Integrating semiconductors with carbon nanomaterials such as carbon nanotubes, graphene oxide, and carbon dots has recently been proposed a promising strategy to enhance the performance of the main photocatalyst [16,17]. Carbon dots, a new class of nano-carbon with sizes below 10 nm, have been of particular interest owing to their unique photoluminescence (PL) up-conversion, as well as photoinduced electron transfer properties [18,19]. Hybrid structures of ZnO and

* Corresponding author.

E-mail address: pbiswas@wustl.edu (P. Biswas).

carbon dots have been demonstrated to exhibit superior photocatalytic performance to their pristine ZnO counterparts under both UV and visible light [20–24]. Nevertheless, their photocatalytic behavior in the NIR region has not been reported yet. Here we pursue the idea that coupling ZnO_{1-x} with carbon dots could be a rational strategy to extend the photo-response of ZnO_{1-x} into the NIR region to further improve CO_2 photoreduction.

An aerosol-assisted synthesis of ZnO_{1-x} /carbon dots hollow composites ($\text{ZnO}_{1-x}/\text{C}$) and their application in photocatalytic CO_2 reduction over a broad UV–vis–NIR spectrum is reported for the first time. The $\text{ZnO}_{1-x}/\text{C}$ composites were produced by a single-step furnace aerosol reactor (FuAR) technique. This continuous flow method is simple and rapid with high throughput, which allows an easy scale-up of the synthesis [25–27]. A series of $\text{ZnO}_{1-x}/\text{C}$ composites were synthesized by controlling the precursor component ratio and synthesis temperature. The composites were characterized in detail, and their performance for CO_2 photoreduction was analyzed under UV, visible and NIR region. The results demonstrated that the photocatalytic response of $\text{ZnO}_{1-x}/\text{C}$ composite was successfully extended to the NIR region without involving any noble metals. To the best of our knowledge, this is the first study reporting a NIR light active $\text{ZnO}_{1-x}/\text{C}$ composite photocatalyst for CO_2 reduction.

2. Experimental section

2.1. Materials

All materials were of analytical grade and used as received without further purification. Zinc nitrate hexahydrate and citric acid were obtained from Sigma-Aldrich (St. Louis, MO). CHO (CCL-61™) (Chinese hamster ovary) cells were purchased from American Type Culture Collection (Manassas, VA). SlowFade™ gold antifade mountant with DAPI (4',6-diamidino-2-phenylindole) nuclear stain was purchased from Thermo Fisher Scientific (Waltham, MA). LIQUION™ Nafion™ containing solution was purchased from Ion Power Nafion™ Store (Newcastle, DE). Alumina micropolish powder (0.05 μm) was obtained from Buehler (Lake Bluff, IL).

2.2. Synthesis of $\text{ZnO}_{1-x}/\text{C}$ composite

The $\text{ZnO}_{1-x}/\text{C}$ composites were synthesized in a lab-built FuAR depicted in Fig. S1a. The precursor solution contained 0.5 M of zinc nitrate hexahydrate and various concentrations of citric acid (CA) in deionized (DI) water. The solution mixture was stirred for 1 h before using it. Then, the precursor solution was nebulized into aerosol droplets using a Collison nebulizer (BGI Incorporated), and the droplets were carried by nitrogen gas (12 psi) through a quartz tube (1 mm X 25 mm ID) heated to various temperatures. The products were collected downstream of the reactor on a glass fiber membrane filter. The synthesized samples were denoted $\text{ZnO}_{1-x}/\text{C}(\text{Y})$, where Y corresponds to the molar ratio of CA/Zn in the precursor solution.

For comparison, a pure ZnO sample was prepared by annealing the $\text{ZnO}_{1-x}/\text{C}(0.6)$ sample at 600 °C in air for 3 h, followed by allowing it to cool to room temperature. Additionally, we also prepared the $\text{ZnO}_{1-x}/\text{C}$ with a fixed CA/Zn ratio of 0.6 at different FuAR temperatures (500, 550, 600, and 650 °C) to investigate the temperature effect on the photocatalytic activity of the composites.

2.3. Characterization

The morphology and elemental distribution of zinc, oxygen, and carbon of the synthesized materials were examined by high-resolution transmission electron microscopy – EDX (HR-TEM, JEOL J2100F). The HR-TEM was operated at 200 kV accelerating voltage. The crystal phase of the material was determined by X-ray Diffraction (XRD) (D8 Advance, Bruker, USA) with Cu K α radiation ($\lambda = 1.548 \text{ \AA}$). The optical

properties of the materials were measured using a UV–vis spectrophotometer (UV-2600, Shimadzu, USA). The surface chemical properties were analyzed by laser Raman spectrometry (Renishaw InVia Reflex confocal Raman spectrometer, with a 514 nm laser) and X-ray photoelectron spectroscopy (XPS) (PHI 5000 VersaProbe II) equipped with a monochromatic Al K α (1486.6 eV) X-ray source. The surface area and pore size distribution were analyzed using the nitrogen physisorption method. In total, 79 adsorption and desorption points were analyzed using the nitrogen physisorption method (Autosorb-1, Quantachrome Instruments, Boynton Beach, FL). The surface area was calculated using the Brunauer–Emmett–Teller (BET) method and the pore size distribution was evaluated by non-local density functional theory (NLDFT).

The thermal behavior of the as-synthesized materials was analyzed by thermal gravimetric and differential thermal analyses (TGA/DTA) (TA Instruments, New Castle, DE). The CO_2 adsorption tests were conducted by the same TGA analyzer. Typically, the powder samples were loaded on the TGA sample holder and purged with nitrogen gas at 120 °C with a flow rate of 25 cm^3/min for 30 min, by which time the weight remained unchanged, which strongly implied that the evaporation of water from the samples was complete. The mass change of the samples during CO_2 adsorption was then recorded under an isothermal condition of 30 °C. The inlet CO_2 concentration was 99.999% (v/v in N_2), which was obtained from a certified gas cylinder and introduced at a flow rate of 25 cm^3/min for 15 min of adsorption, after which the weight remained unchanged, ensuring that the adsorbents were completely saturated. The fluorescence spectra of synthesized materials were recorded using a Vis-NIR spectrofluorometer (Horiba Jobin Yvon Inc). Samples were diluted until clear and sonicated for at least 5 min before the measurements. At least three measurements per sample were taken. Fluorescence lifetime was measured using time-correlated single-photon counting (TCSPC) method on Fluorolog (Horiba) equipped with a PMT928P detector and imaging spectrometer iH320. Data Station software (Horiba) was used for data acquisition. Samples were diluted in MilliQ water and sonicated. Lifetime measurements were conducted at 295 nm excitation NanoLED light sources at 1 MHz frequency and slit width of 8 nm. Ultraviolet photoemission spectroscopy (UPS) measurements, using Physical Electronics 5000 VersaProbe II Scanning ESCA Microprobe, were performed to determine the valence band, conduction band and Fermi level position. He I (21.2 eV) ultraviolet source was used, and 5 V bias was applied to the sample to observe a clear secondary electron edge. The samples were prepared on Si wafer coated with ~15 nm gold film. Fourier transform infrared (FTIR) spectra of all the samples were recorded via a Nicolette Nexus 470 FTIR spectrometer.

2.4. In-vitro imaging analysis with confocal microscopy

To examine the photo-excitability of ZnO and $\text{ZnO}_{1-x}/\text{C}(0.6)$ samples, confocal microscopy was performed. Chinese hamster ovary (CHO) cells were seeded in CELLview™ plates at 5×10^4 cells/well and allowed to grow for 24 h. After another 24 h of exposure to the synthesized materials, the cells were fixed and washed with phosphate buffer saline (PBS) three times before imaging. All cells were fixed by immersion in 4% paraformaldehyde (PFA) as the cross-linking solution for 10 min at room temperature. The cells were then washed three times with ice-cold 1x PBS for 3 min each time. The fixed cells were incubated in ice-cold 1x PBS buffer containing 0.1% Triton (permeabilization agent) for 10 min at room temperature, then washed three times with ice-cold 1x PBS for 5 min each time. The CELLview™ plates were then incubated with blocking buffer for 30 min. To stain the nuclei, SlowFade™ gold antifade mountant with DAPI (diluted 1:100 in 1x PBS) was used. The cells were incubated overnight at 4 °C. During confocal microscopy analysis, the laser wavelengths were 405 nm for DAPI (nucleus staining), and 405, 488, 532, and 635 nm for materials detection. A negative control sample (untreated cells) was prepared

with cells in the absence of hollow spheres.

2.5. Photoelectrochemical measurements

Photoelectrochemical measurements were performed using a lab-built three-electrode cell setup with a Pt wire as the counter electrode and an Ag/AgCl bar as the reference electrode. For the working electrode, 5 mg of the material powder was dispersed in 0.75 ml of DI water, followed by the addition of 20 μ l of Nafion solution (0.05%, Sigma-Aldrich). After approximately 40 min of ultrasonication, the above suspension was dropped onto the surface of an indium tin oxide (ITO) conductor glass slide, whose the contact side had previously been protected using Teflon tape. The working electrode was then dried at 60 °C for 4 h. The photocurrent was measured using a CHI 760 Bipotentiostat in 0.1 M Na₂SO₄ solution.

2.6. Photocatalytic activity evaluation

Gas-phase photocatalytic reduction of CO₂ by H₂O vapor was performed using a lab-built stainless steel reactor operating in continuous flow mode, as shown in Fig. S1b. For each test, 15 mg of catalyst was uniformly dispersed onto a membrane filter and placed in the photoreactor. High purity CO₂ (99.999%, Praxair) was continuously passed through a water bubbler to obtain a gas mixture of CO₂ + H₂O, which then flowed into the photoreactor. Prior to each reaction test, a high gas flow rate (16.0 ml min⁻¹) of CO₂ was used to purge air from the reactor for 35 min, and then a flow rate of 3.0 ml min⁻¹ was maintained during the whole 5 h photoreaction. A 400 W Xe Arc lamp (Oriel 66021, Newport Co.) equipped with different cut-off filters was employed to provide radiation in different wavelength regions, including UV-vis-NIR (250–950 nm), Vis-NIR (400–950 nm), and NIR (715–950 nm). The light spectra with different cut-off filters are shown in Fig. S2. The gaseous products (CH₄, CO₂, CO, O₂, and N₂) in the reactor effluent were continuously analyzed using a gas chromatograph (GC, 6895N, Agilent Technologies, Inc.) equipped with a thermal conductivity detector (TCD). Helium was used as the carrier gas. Since this study emphasized photocatalytic reduction of CO₂ on a gas-solid interface, possible products such as methanol, formaldehyde, and formic acid were not measured, which are more likely produced in CO₂ photo-reduction in aqueous solutions.

2.7. Isotope experiment for CO₂ photoreduction

Isotope experiments were performed in the same reactor under the whole UV-vis-NIR spectrum. ¹³CO₂ (Sigma-Aldrich) was used as the source gas. The products in the reactor after 3 h light irradiation were analyzed by a GC (7890A, Agilent Technologies, Inc.), equipped with an Agilent J&W GS-CarbonPLOT capillary column (0.32 mm ID, 3 μ m film thickness, and 60 m length), and a mass spectrometer (5975C, Agilent Technologies, Inc.).

3. Results and discussion

3.1. Synthesis and formation of ZnO_{1-x}/C

Scheme 1 illustrates the formation route of the ZnO_{1-x}/C composite hollow sphere. The formation of ZnO_{1-x}/C through the FuAR process is based on a “droplet-to-particle” mechanism [28]. First, the precursor solution was atomized to form small aerosol droplets. The droplets were carried through the high temperature (600 °C) furnace by nitrogen carrier gas. During the flight, CA/Zn(NO₃)₂ precipitates were formed after the complete drying of aerosol droplets. Afterward, the ZnO/C composites were formed as the result of the decomposition of Zn(NO₃)₂ and the carbonization of citric acid. Under the nitrogen atmosphere, the pyrolysis of citric acid produced solid carbon and a large amount of reducing gasses (e.g., CH₄, CO, and H₂) [29], which then created an

outward “blowing force,” leading to the formation of a hollow sphere. Both the deposited carbon and the reducing gases participated in the reduction reactions of ZnO to ZnO_{1-x} particles. It should be mentioned that no carbonaceous products were formed when only citric acid was used as the precursor under the same conditions, implying that transition metal Zn served as a nucleation site for carbonization of citric acid to form carbon materials. Also, the hollow structures were formed only in the presence of both zinc nitrate and citric acid precursors. Thus, citric acid not only serves as a reducing agent and carbon source but also supports the formation of hollow structure. Given the roles of zinc nitrate and citric acid, the number of oxygen vacancies and deposited carbon in the ZnO_{1-x}/C composite could be easily controlled by altering the CA/Zn ratio and the FuAR temperature.

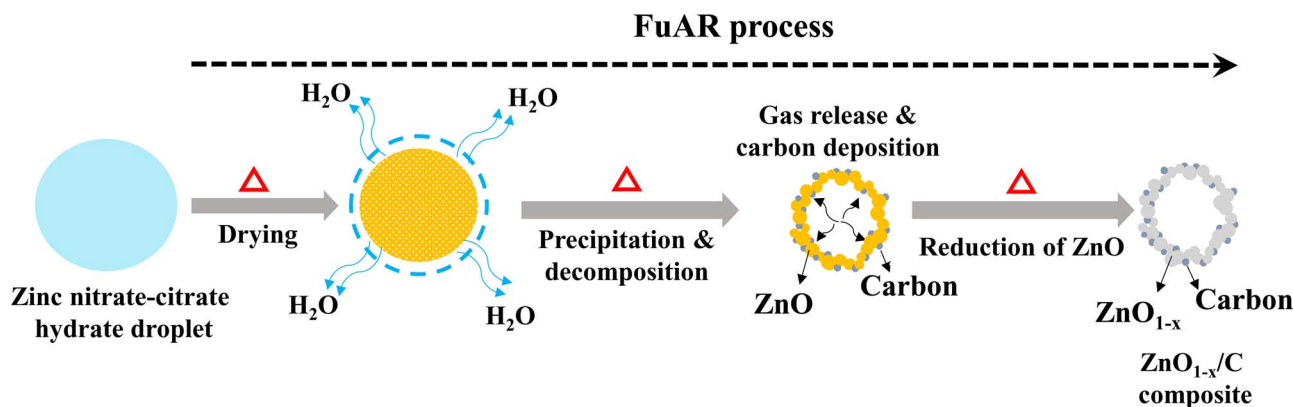
In past years, several strategies have been reported for developing oxygen-deficient metal oxide semiconductors, such as hydrogen thermal treatment [30] and metal reduction using Mg and Al under a hydrogen/argon atmosphere [31,32]. Nevertheless, the need to carefully control the hydrogenation treatment procedures and the high-pressure conditions make the manufacturing process rather difficult, expensive, and time-consuming. Besides, solvent-intensive washing processes are also required to remove the reactive metals from the synthesized materials thoroughly. In contrast, the continuous and scalable FuAR process synthesizes ZnO_{1-x}/C composites in a very short residence time of only a few seconds, without involving extra hydrogen gas or any post thermal or washing treatment.

3.2. Characterization of ZnO_{1-x}/C

The morphology of the ZnO_{1-x}/C(0.6) composite was characterized using HR-TEM technique. As displayed in Fig. 1a, the ZnO_{1-x}/C(0.6) composite particles retain the spherical morphology of the atomized precursor droplets, and the hollow structure is verified by the bright contour at the center of the spheres. An HR-TEM image (Fig. 1b) also shows a well-crystallized ZnO structure, and the selected area electron diffraction (SAED) pattern (Fig. 1c) further confirms a high crystallinity of ZnO_{1-x}/C(0.6) composite with a hexagonal wurtzite structure, in which six diffraction rings perfectly correspond to the same positions as those from bulk ZnO [33,34]. The EDS elemental mapping images (Fig. 1d–g) of an individual ZnO_{1-x}/C(0.6) composite further indicate that the zinc, oxygen, and carbon are uniformly distributed throughout the whole particle. To confirm the size of the deposited carbon, the ZnO_{1-x}/C(0.6) sample was soaked in 3.0 M HCl solution under stirring for 2 h to remove the ZnO_{1-x}. After treated with acid, the residual carbons are apparently free of zinc elements (Fig. S3). Fig. 1h shows the HR-TEM image of the Zn-free C(0.6), in which well-dispersed nanoparticles with sizes around 2 nm are clearly observed. Moreover, the in-plane spacing in a single carbon dot was estimated to be \approx 0.21 nm (Fig. 1i), which corresponds to the (100) diffraction plane spacing of graphitic carbon [35].

The phase composition and crystallinity of the samples were investigated by XRD (Fig. 2). The powders prepared using zinc nitrate precursor only are identified as mixed phases of wurtzite ZnO structure and zinc nitrate hydroxide hydrate [36]. Similar diffraction reflections are also found on the ZnO_{1-x}/C(0.25). In spite of the high heating experienced by the droplets in the FuAR (600 °C), the low residence time of \approx 9 s in the heated zone was too short for complete decomposition of zinc nitrate. On the contrary, the high phase purity of a typical wurtzite ZnO structure is observed on the ZnO_{1-x}/C samples prepared with higher molar ratios of CA/Zn (0.5–0.75). The results show that adding citric acid in the precursor solution promotes the decomposition of zinc nitrate, and thus improves the crystallinity of the final ZnO_{1-x}/C composites. On the other hand, the diffraction reflections from the wurtzite ZnO structure are more intense and sharper on the pure ZnO sample. This result suggests that post thermal treatment can further enhance the crystallinity of the sample.

The nature of the carbon present in the ZnO_{1-x}/C samples was



Scheme 1. The formation mechanism of the $\text{ZnO}_{1-x}/\text{C}$ composite hollow spheres by the FuAR process.

investigated by Raman spectroscopy (Fig. 3a). All samples possess two peaks at around 1360 and 1585 cm^{-1} , corresponding to the defect-induced feature (D band) and the sp^2 -hybridized carbon within the hexagonal graphitic structure (G band), respectively [37]. The density of defects in graphite materials is commonly expressed by the I_D/I_G (the intensity of the D-band divided by the intensity of the G-band). The value of I_D/I_G decreases from 0.75 ($\text{ZnO}_{1-x}/\text{C}(0.25)$) to 0.55 ($\text{ZnO}_{1-x}/\text{C}(0.75)$) (Table S1), indicating an improved graphitization degree of $\text{ZnO}_{1-x}/\text{C}$ with increased concentration of citric acid. The high graphitization degree improves the electrical conductivity, facilitates favorable electron transport, and therefore enhances photocatalytic performance [38].

Raman spectroscopy was also used to identify the oxygen-deficient nature of the $\text{ZnO}_{1-x}/\text{C}$ samples, and pure ZnO was studied as a reference. As illustrated in Fig. 3b, all the samples demonstrate an intense peak at 435 cm^{-1} , corresponding to the wurtzite phase of ZnO [13]. Compared to the $\text{ZnO}_{1-x}/\text{C}$ samples, the reference ZnO sample shows a sharper peak, suggesting its stronger crystallinity, supporting the XRD results. Another intense peak at 580 cm^{-1} is observed for the $\text{ZnO}_{1-x}/\text{C}$ samples, ascribed to the presence of defect-induced oxygen vacancies [13]. The intensity of this peak increases with an increase in the CA/Zn ratio, suggesting an increase in the number of oxygen vacancies as well. The maximum intense peak at 580 cm^{-1} was obtained for the $\text{ZnO}_{1-x}/\text{C}(0.75)$, indicating the highest number of oxygen vacancy defects among all samples.

Fig. 3c shows the C 1s peak of the XPS spectrum of $\text{ZnO}_{1-x}/\text{C}(0.6)$, which can be fitted into four peaks. The peaks at 284.8 , 285.4 , and 288.7 eV are mainly attributed to amorphous C–C bonding, C–OH and –COOH, respectively [39]. Another peak at 284.2 eV can be assigned to the C=C bond in the graphitic-phase carbon, originating from the carbonization of citric acid [39]. Fig. 3d displays the O 1s spectra of the ZnO, $\text{ZnO}_{1-x}/\text{C}(0.6)$, and $\text{ZnO}_{1-x}/\text{C}(0.75)$ samples. The peak centered at the band energies of about 528.2 eV originates from the lattice oxygen anions (O_I), whereas the peak at 529.6 eV is ascribed to oxygen vacancy defect (O_{II}). The ratios of the areas of O_{II} and O_I were calculated to be 15% , 44.6% and 53.2% for ZnO, $\text{ZnO}_{1-x}/\text{C}(0.6)$, and $\text{ZnO}_{1-x}/\text{C}(0.75)$. The result indicates that $\text{ZnO}_{1-x}/\text{C}(0.75)$ had the highest number of surface oxygen vacancies. Both the Raman and XPS results confirmed the presence of a higher number of oxygen vacancy defects for the $\text{ZnO}_{1-x}/\text{C}$ composites than for pure ZnO. Oxygen vacancies act as a donor and supply electron to the conduction band, hence improving photocatalytic performance [32].

The carbon content of the $\text{ZnO}_{1-x}/\text{C}$ composites was determined by thermogravimetric analysis in air. As seen in Fig. S6a, the $\text{ZnO}_{1-x}/\text{C}(0.25)$ sample showed weight losses over a broad temperature range (100 – 400°C). It is noted in the DTA profile (Fig. S6b) that, compared with other $\text{ZnO}_{1-x}/\text{C}$ samples, $\text{ZnO}_{1-x}/\text{C}(0.25)$ undergoes a significant weight change at 155°C . This weight loss is related to the thermal decomposition of zinc nitrate hydroxide hydrate, which was reported to

thermally decompose over a temperature range of 65 – 240°C [40].

Contrarily, the decomposition of the $\text{ZnO}_{1-x}/\text{C}$ samples, with a high citric acid concentration, occurs in a single sharp weight loss between 300 to 500°C , with a pronounced primary weight loss at 400 – 410°C (Fig. S6b). This weight loss is due to the complete combustion of deposited carbons in the samples. The total carbon is calculated from the weight difference over the temperature range of 300 to 500°C (Table S1). Obviously, the higher the concentration of citric acid in the precursor solutions, the larger the amount of carbon present in the final $\text{ZnO}_{1-x}/\text{C}$ products. A slight increase in the mass between 500 to 700°C is observed for all the $\text{ZnO}_{1-x}/\text{C}$ composites, except for $\text{ZnO}_{1-x}/\text{C}(0.25)$. This increase could be due to the oxidation of ZnO_{1-x} to ZnO under air flow. In particular, $\text{ZnO}_{1-x}/\text{C}(0.75)$ had the largest mass increase ($\sim 1.07\%$), followed by $\text{ZnO}_{1-x}/\text{C}(0.6)$ ($\sim 0.28\%$), and $\text{ZnO}_{1-x}/\text{C}(0.5)$ ($\sim 0.1\%$). As a result, these findings clearly confirm the presence of oxygen vacancies in the $\text{ZnO}_{1-x}/\text{C}$ composites.

Fig. S7a shows the nitrogen physisorption isotherms of the pristine ZnO and $\text{ZnO}_{1-x}/\text{C}$. All samples possess a hysteresis loop over a P/P_0 range of 0.3 – 1.0 , characteristic of mesoporous structure [5]. This structure is further confirmed by the NLDFT pore size distribution plots (Fig. S7b), in which a broad range of pore size distributions (2 – 25 nm) is clearly observed. The BET specific surface area (S_{BET}) and total pore volume (V_p) of the samples are summarized in Table S1. The S_{BET} and V_p of the $\text{ZnO}_{1-x}/\text{C}$ samples are significantly larger than that of the pure ZnO. Besides, for the $\text{ZnO}_{1-x}/\text{C}$ samples, the specific surface area of the samples increases slightly with an increased molar ratio of CA/Zn. Generally, a photocatalyst with the high surface area and high adsorption ability toward target reactants contributes to higher photocatalytic activity by allowing more reactant molecules to be adsorbed onto the catalyst surface [5]. In this sense, we expect that this unique $\text{ZnO}_{1-x}/\text{C}$ hollow composite with a large surface area will provide more active sites for CO_2 adsorption, thus enhancing CO_2 photoreduction.

3.3. Photocatalytic activity evaluation for CO_2 photoreduction

Photoreduction of CO_2 with H_2O on the $\text{ZnO}_{1-x}/\text{C}$ composites was conducted in a continuous flow reactor at ambient temperature and atmospheric pressure. Prior to that, three preliminary control tests were performed under the following conditions: (1) in the absence of a catalyst, (2) in the absence of light illumination, and (3) in the absence of CO_2 . As displayed in Fig. S8, no carbonaceous product was detected in all cases, confirming the absence of CO_2 photoreduction on the $\text{ZnO}_{1-x}/\text{C}$ composites. However, in the presence of all the three necessary components (catalyst, light source, and $\text{CO}_2 + \text{H}_2\text{O}$), only CO was detected. This result shows that CO was formed from the photoreduction of CO_2 , and rules out the possibility of photolysis and decomposition of surface carbons on the $\text{ZnO}_{1-x}/\text{C}$ composites [41]. Also, isotope tracer analyses using $^{13}\text{CO}_2$ were conducted for the $\text{ZnO}_{1-x}/\text{C}$

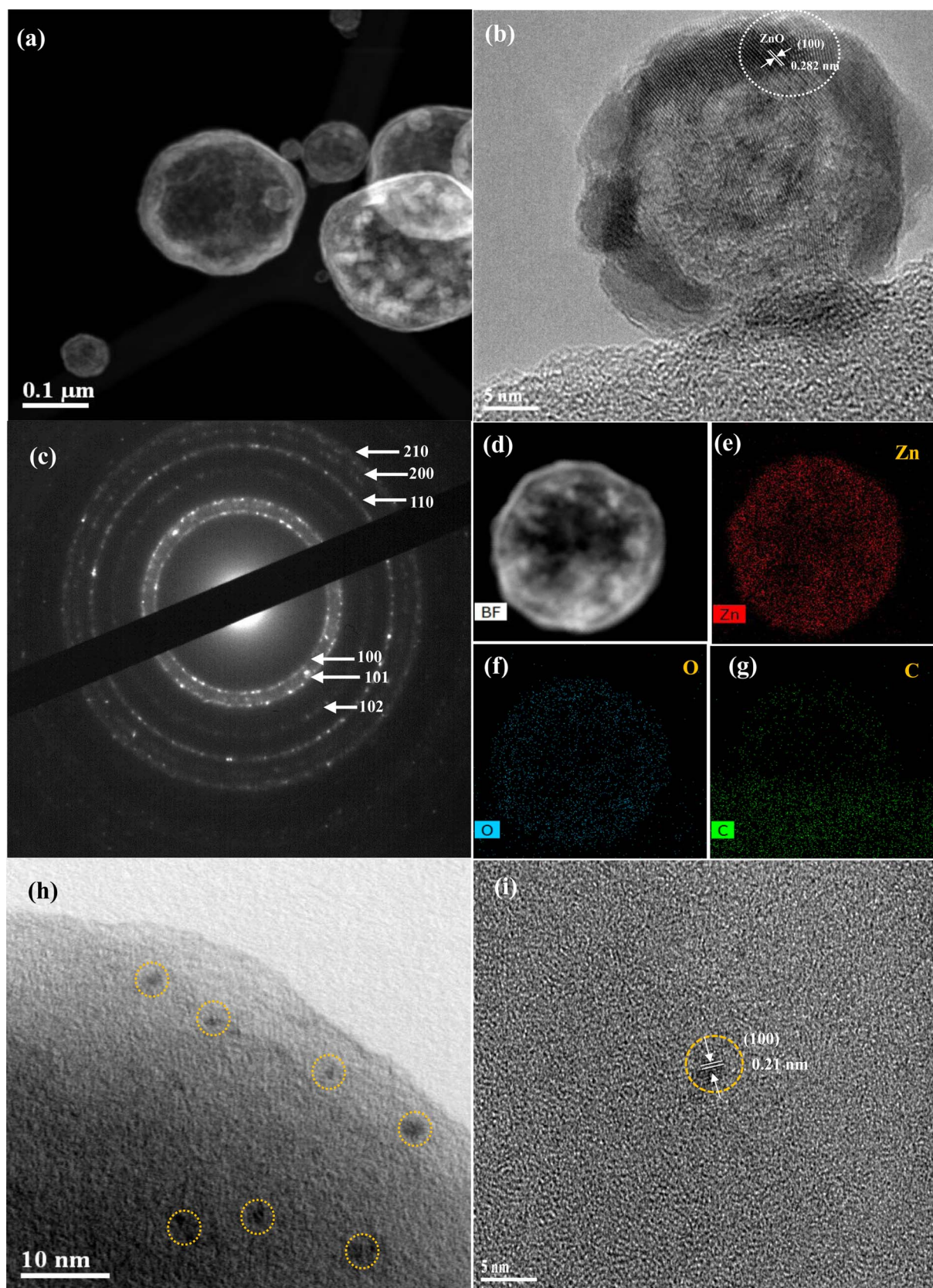


Fig. 1. (a,b)HR-TEM images, (c) SAED pattern, (d–g) EDS elemental mapping images of the ZnO_{1-x}/C(0.6) and (h,i) HR-TEM images of Zn-free C(0.6).

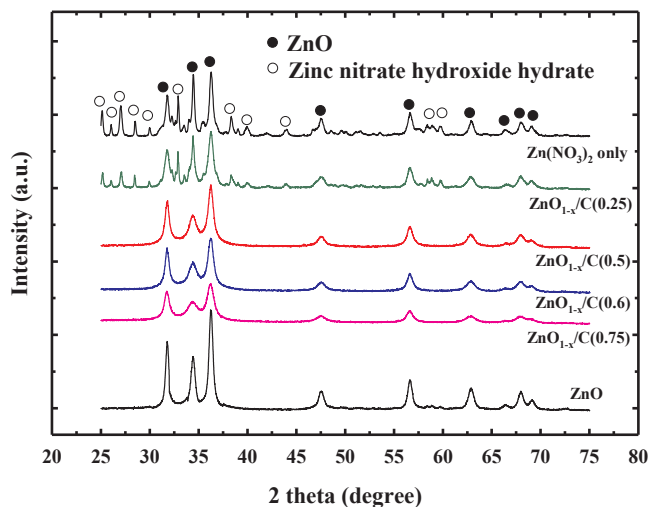


Fig. 2. XRD patterns of ZnO and $\text{ZnO}_{1-x}/\text{C}$ composites.

C(0.6) sample. Fig. S9 shows the gas and mass chromatography spectra of the gas samples in the reactor, with the $\text{ZnO}_{1-x}/\text{C}(0.6)$ sample under irradiation by the whole UV–vis–NIR spectrum for 3 h. To exclude the effect of nitrogen gas (remaining in the column) in the mass chromatography analysis, which has a similar retention time and m/z value of

CO, selected ion monitoring of compositions with m/z value as 12 and 13 were conducted. A significant peak corresponding to ^{13}C at a retention time of 4.13 min (the retention time of CO) was detected, which verified that the CO originated from CO_2 , not from the decomposition of the catalysts.

It is well known that the photoreduction of CO_2 is a proton-assisted multi-electron transfer process [16]. In this process, even though the production of hydrocarbons (e.g., methanol, formaldehyde, and ethanol) is thermodynamically favorable, it requires more electrons and protons, thus encountering kinetic limitations. Furthermore, these products are more likely produced in CO_2 photoreduction in aqueous solutions [42]. Since this study focused on the CO_2 reduction on a gas-solid interface, CO was found as the main product in our flow reactor system because it needs a minimum number of electrons and protons and appears to be kinetically favorable. The absence of CH_4 in this study could reflect the fact that more electrons and protons are required to reduce CO_2 to CH_4 , making it more difficult to generate than CO. For producing CH_4 , an eight-electron reduction and available H atoms from the oxidation of water on the same catalyst surface are required [3]. If the CO desorbs from the surface before it can be fully reduced, then the formation of CH_4 is significantly affected.

To understand the light-harvesting behaviors of the photocatalysts, we performed photocatalytic tests under different wavelength ranges, including UV–vis–NIR (250–950 nm), Vis–NIR (400–950 nm), and NIR (715–950 nm). Fig. 4a compares the average CO production rate of various photocatalysts for 5 h. For each catalyst, experiments were

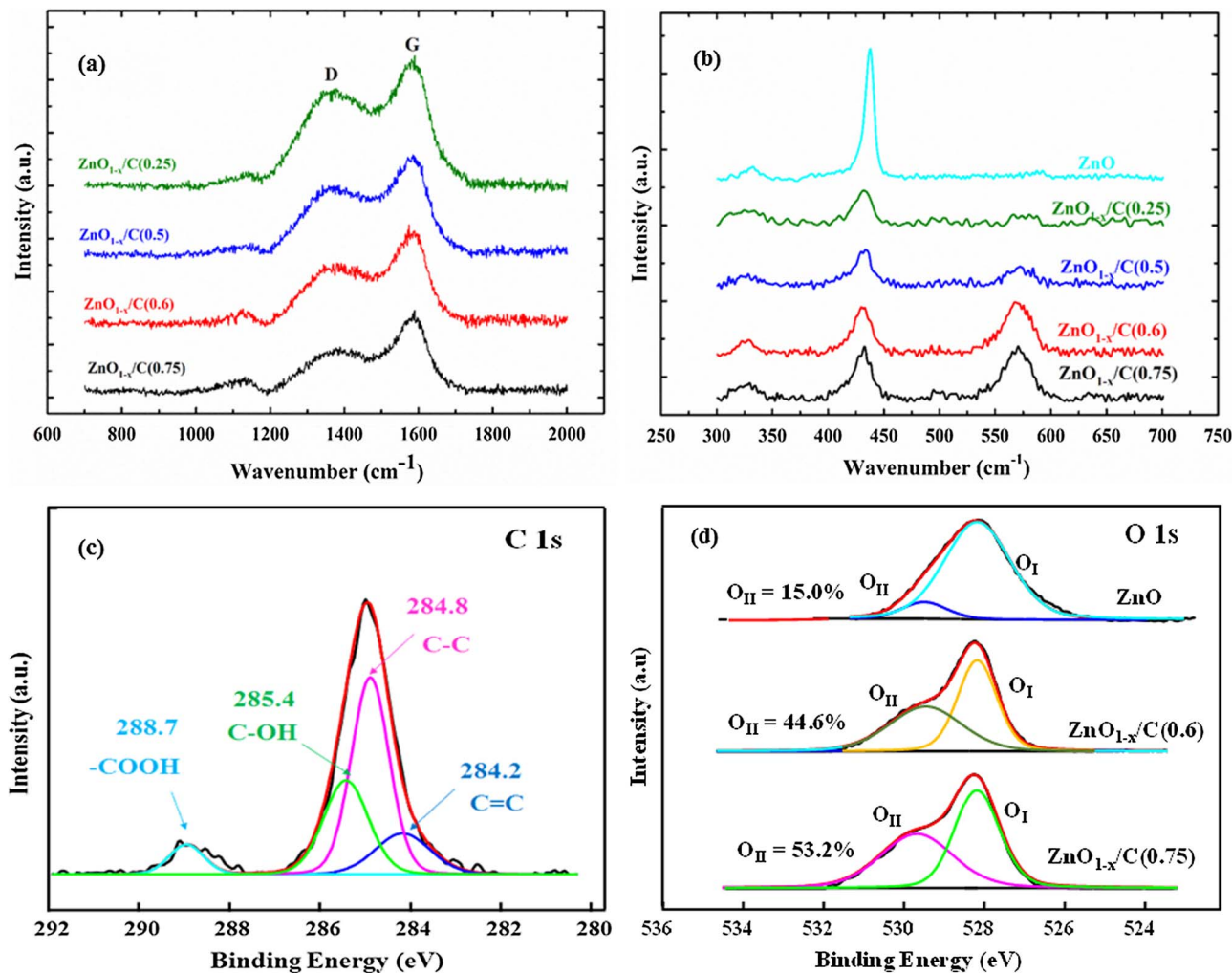


Fig. 3. Raman spectra of ZnO and $\text{ZnO}_{1-x}/\text{C}$ composites (a) carbon (b) ZnO, (c) C 1s spectrum of $\text{ZnO}_{1-x}/\text{C}(0.6)$, and (d) O1s XPS spectra of ZnO, $\text{ZnO}_{1-x}/\text{C}(0.6)$ and $\text{ZnO}_{1-x}/\text{C}(0.75)$ composites.

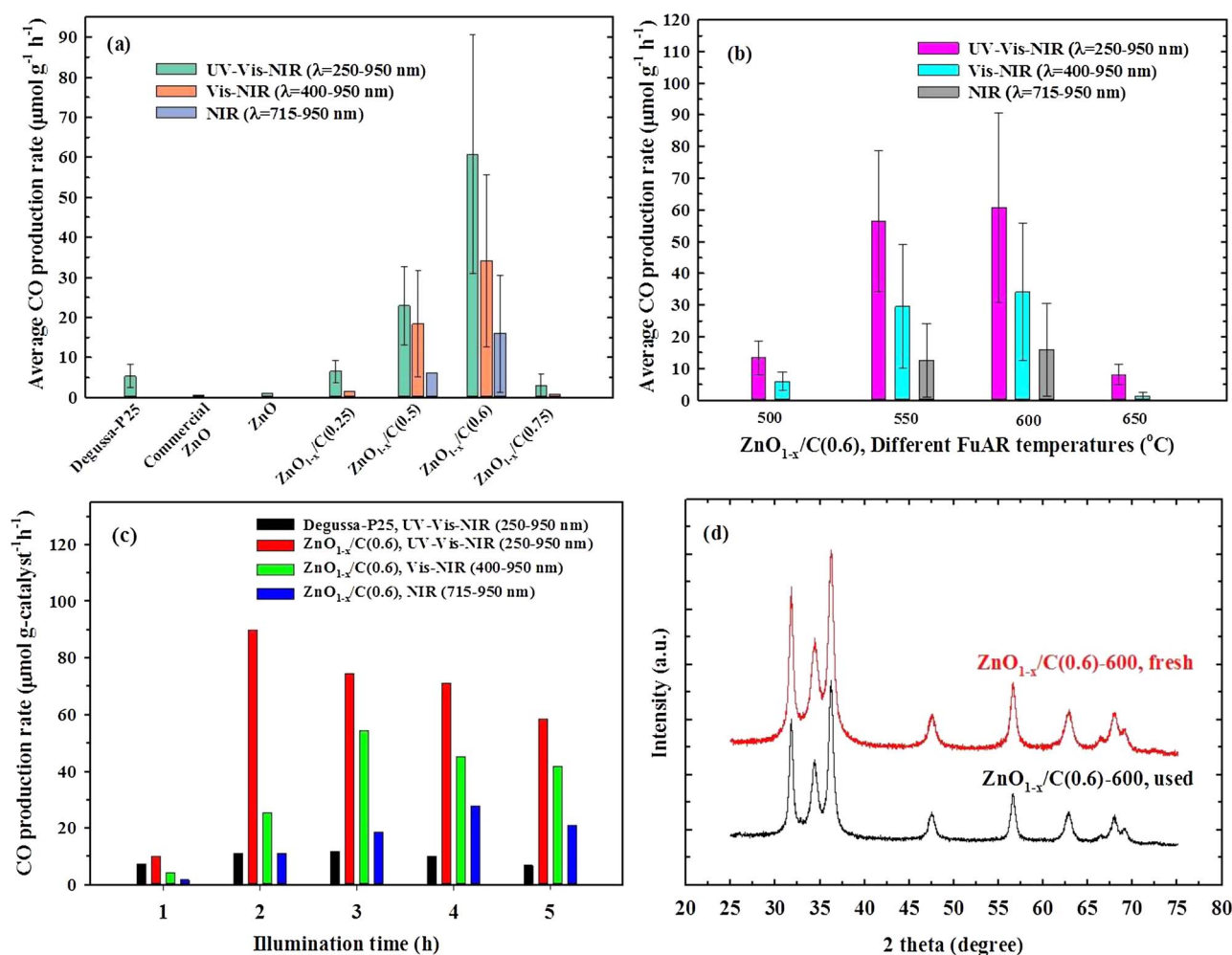


Fig. 4. (a) Average production rate of CO (5 h) on $\text{ZnO}_{1-x}/\text{C}$ samples synthesized with different concentration of citric acid, FuAR temperature: 600 °C, (b) Average production rate of CO (5 h) on $\text{ZnO}_{1-x}/\text{C}(0.6)$ synthesized at different FuAR temperatures, (c) Time-dependent production rate of CO on the Degussa-P25 and $\text{ZnO}_{1-x}/\text{C}(0.6)$ composite under different wavelength ranges, and (d) XRD patterns of the fresh and used $\text{ZnO}_{1-x}/\text{C}(0.6)$ composite.

repeated twice using fresh catalysts, and the production rates were averaged and standard deviations reported. Commercial ZnO and FuAR-synthesized ZnO show CO production rates of 0.61 and 1.11 $\mu\text{mol g}^{-1} \text{h}^{-1}$, respectively, under UV-vis-NIR irradiation. Compared to the ZnO samples, the CO production rate of the $\text{ZnO}_{1-x}/\text{C}$ composites were considerably larger. The highest CO production rate was observed on $\text{ZnO}_{1-x}/\text{C}(0.6)$, with an average value of 60.77 $\mu\text{mol g}^{-1} \text{h}^{-1}$, which is a more than 54-fold enhancement in CO production over that of pristine ZnO. TiO_2 (Degussa-P25) is a well-known benchmark photocatalyst and has been extensively investigated for CO_2 photoreduction [43,44]. For comparison, we measured the photocatalytic activity of Degussa-P25 for CO_2 photoreduction in identical conditions under the UV-vis-NIR irradiation. The average CO production rate of Degussa-P25 is 5.30 $\mu\text{mol g}^{-1} \text{h}^{-1}$, 11.5 times lower than that of $\text{ZnO}_{1-x}/\text{C}(0.6)$.

Furthermore, we investigated that catalytic performance in the Vis-NIR and NIR regions. Both ZnO and Degussa-P25 are photocatalytically inactive. On the contrary, all the $\text{ZnO}_{1-x}/\text{C}$ composite are active for CO_2 photoreduction under Vis-NIR irradiation, in the order of $\text{ZnO}_{1-x}/\text{C}(0.6) > \text{ZnO}_{1-x}/\text{C}(0.5) > \text{ZnO}_{1-x}/\text{C}(0.25) > \text{ZnO}_{1-x}/\text{C}(0.75)$ (Fig. 4a). More significantly, only the $\text{ZnO}_{1-x}/\text{C}(0.5)$ and $\text{ZnO}_{1-x}/\text{C}(0.6)$ are active in only NIR region. Again, the $\text{ZnO}_{1-x}/\text{C}(0.6)$ outperforms other samples in both Vis-NIR (400–950 nm) and NIR (715–950 nm) photocatalytic activity, with average CO production yields of 34.17 and 15.98 $\mu\text{mol g}^{-1} \text{h}^{-1}$, respectively, which was achieved without involving any noble metals. These results clearly suggest the superiority of $\text{ZnO}_{1-x}/\text{C}(0.6)$ composite in harnessing low-energy NIR

photons to reduce highly stable CO_2 to CO. Moreover, CO yield was further optimized by varying the FuAR temperature from 500–650 °C (Fig. 4b). $\text{ZnO}_{1-x}/\text{C}(0.6)$ composite synthesized at 550 and 600 °C showed higher photocatalytic activity than composites synthesized at 500 and 650 °C. Based on the above results, we conclude that both the precursor component ratio and FuAR temperature had strong impacts on the photocatalytic performance of $\text{ZnO}_{1-x}/\text{C}$ composites for CO_2 reduction.

In Table S2, the photocatalytic performance of $\text{ZnO}_{1-x}/\text{C}(0.6)$ is compared with previously reported results under similar conditions. Our CO productivities are considerably higher than the reported values for diverse inorganic heterostructure photocatalysts. The quantum efficiency based on CO production over $\text{ZnO}_{1-x}/\text{C}(0.6)$ was calculated to be 0.13% under UV-vis light (see Supporting information for detailed calculations), which is 3, 37, 9, 18, and 13 times higher than reported for V-W- TiO_2 (QY = 0.039%), ZnO-CuO (QY = 0.0035%), reduced TiO_{2-x} (QY = 0.0141%), NiGO- TiO_2 (QY = 0.0072%) and EDA-rGO- TiO_2 (QY = 0.0094%), respectively. It is worth mentioning that our engineered material did not employ any noble metal cocatalyst or doping of foreign elements. It is therefore anticipated that hetero-integration or doping in our future work may result in an even more promising photocatalyst for visible- and NIR-driven CO_2 reduction.

Fig. 4c shows the production rates of CO on Degussa-P25 and $\text{ZnO}_{1-x}/\text{C}(0.6)$ as a function of illumination time under different wavelength ranges. For both catalysts, the production rates tend to decrease after reaching the maximum values. It is well-known that

photocorrosion of ZnO occurs easily, which reduces its photocatalytic stability [10]. The changes in the phase composition caused by the photocatalytic reaction were investigated by XRD (Fig. 4d). No significant difference was observed in the XRD results between fresh and used $\text{ZnO}_{1-x}/\text{C}(0.6)$ samples. Moreover, the oxygen vacancy defect of the used $\text{ZnO}_{1-x}/\text{C}(0.6)$ was also investigated and compared with the fresh one, with the results presented in Fig. S10. The obtained O1s spectrum of the used $\text{ZnO}_{1-x}/\text{C}(0.6)$ was deconvoluted into three peaks. Different from the fresh $\text{ZnO}_{1-x}/\text{C}(0.6)$, the used one shows an additional peak, which can be assigned to the adsorbed H_2O on the catalyst. This observation reflects the adsorption of a large amount of water vapor on the catalyst surface during the photoreaction. Nevertheless, the ratio of the areas of O_{II} (oxygen vacancy defect) and O_{I} (lattice oxygen) was calculated to be 43.0%, which is almost identical to that of the fresh sample (44.6%). The above results clearly indicate high structural and chemical stability of the $\text{ZnO}_{1-x}/\text{C}(0.6)$. The declined photocatalytic activity has been commonly reported in gas-phase photoreduction of CO_2 operated in a continuous mode [3,43,45]. It is believed that the deterioration was ascribed to the coverage and saturation of the active sites with less reactive intermediates on the surface of the photocatalysts, and hindered the photocatalytic reactions [16].

3.4. Mechanism of photocatalytic enhancement

3.4.1. CO_2 uptake

Adsorption of CO_2 on the surface of the catalyst is the first step in the photocatalytic reaction. Hence it is an important parameter for evaluating the performance of the catalyst [46]. Fig. 5a represents the time-dependent CO_2 uptake of ZnO and $\text{ZnO}_{1-x}/\text{C}$ samples, evaluated by the TGA measurement. The ZnO shows a low adsorption uptake of 0.0095 mmol- CO_2 /g-sample, whereas all the $\text{ZnO}_{1-x}/\text{C}$ samples have considerably improved CO_2 uptakes, in the order of $\text{ZnO}_{1-x}/\text{C}(0.75)$ (0.32 mmol- CO_2 /g) \approx $\text{ZnO}_{1-x}/\text{C}(0.6)$ (0.31 mmol- CO_2 /g) $>$ $\text{ZnO}_{1-x}/\text{C}(0.5)$ (0.27 mmol- CO_2 /g) $>$ $\text{ZnO}_{1-x}/\text{C}(0.25)$ (0.08 mmol- CO_2 /g). The increased CO_2 adsorption could result from the large surface area of the $\text{ZnO}_{1-x}/\text{C}$ samples. Interestingly, after normalization by their surface area, the adsorption abilities of the $\text{ZnO}_{1-x}/\text{C}$ samples are still 3.42 ($\text{ZnO}_{1-x}/\text{C}(0.75)$), 3.34 ($\text{ZnO}_{1-x}/\text{C}(0.6)$), 3.15 ($\text{ZnO}_{1-x}/\text{C}(0.5)$), and 1.51 ($\text{ZnO}_{1-x}/\text{C}(0.25)$) times that of ZnO. Therefore, the improved CO_2 adsorption of the $\text{ZnO}_{1-x}/\text{C}$ cannot be explained by the increased surface area alone, but probably is also associated with the amounts of deposited carbon and oxygen vacancy.

A recent work suggested that an oxygen vacancy-rich surface is more thermodynamically favorable for CO_2 capture than a defect-free surface [47]. Xie et al. [48] showed that, compared with stoichiometric SrTiO_3 , the chemical adsorption of CO_2 was improved by increasing the oxygen deficiency in SrTiO_3 , thus leading to enhanced CO_2 photoreduction. Therefore, the presence of oxygen vacancy defects could significantly enhance the adsorption of CO_2 , leading to increasing the photoreduction CO_2 . In this regard, the highest activity of $\text{ZnO}_{1-x}/\text{C}(0.6)$ could also be related to its high CO_2 adsorption capacity, demonstrating the important role of the CO_2 adsorption process in the current reaction scheme. Nevertheless, it is noteworthy that the high CO_2 uptake of $\text{ZnO}_{1-x}/\text{C}(0.75)$ did not guarantee high photocatalytic activity; rather, it showed the poorest activity among all samples. These results indicated that the CO_2 adsorption ability is not the only parameter affecting photocatalytic performance in these catalysts.

3.4.2. Light absorption properties

The light response range is an important evaluation factor in photocatalysis [49]. Fig. 5b displays the diffuse reflectance spectra of ZnO and $\text{ZnO}_{1-x}/\text{C}$ composites. The ZnO shows a steep increase in absorption at wavelengths shorter than ≈ 400 nm, which is due to the intrinsic bandgap absorption of ZnO [13]. Notably, a significantly enhanced absorption in the entire UV–vis–NIR spectrum region

(300–1400 nm) can be observed for the $\text{ZnO}_{1-x}/\text{C}$ samples, accompanied by their gradual color change from white (ZnO) to grayish-black ($\text{ZnO}_{1-x}/\text{C}(0.75)$) (inset of Fig. 5b). The enhanced light absorption is proposed to be due to the presence of oxygen vacancy defects, which decreases the band gap of the material and also creates additional sub-band below the conduction band [13,50]. Moreover, the excellent light harvesting ability of the narrow gap sp^2 carbon present in the deposited carbons can also contribute to enhancing the light absorption in the Vis–NIR region [51]. The excellent light harvesting ability of $\text{ZnO}_{1-x}/\text{C}$ and the utilization of Vis–NIR light promoted the photogeneration of charge carriers, improving the photocatalytic activity of the $\text{ZnO}_{1-x}/\text{C}$ composites.

In-vitro confocal microscopy was demonstrated to assess the excitability of ZnO and $\text{ZnO}_{1-x}/\text{C}(0.6)$ samples at different wavelengths. Fig. 5c displays the confocal microscopy images of CHO cells after 24-hour incubation with 0.5 mg/ml $\text{ZnO}_{1-x}/\text{C}(0.6)$. In a control test (without either ZnO or $\text{ZnO}_{1-x}/\text{C}(0.6)$), no signal was detected (Fig. S11), except for the nuclei which are stained with DAPI and known to fluoresce when excited at 405 nm. For comparison, the confocal microscopy images of CHO cells after 24-hour incubation with 0.5 mg/ml ZnO was performed as well. A weak intracellular luminescence was detected from the CHO cells in the presence of ZnO when excited at 488, 532, and 635 nm (Fig. S12), whereas obvious fluorescence signals were detected inside the cells after exposure of CHO cells to $\text{ZnO}_{1-x}/\text{C}(0.6)$ (Fig. 5c). It is concluded that both ZnO and $\text{ZnO}_{1-x}/\text{C}(0.6)$ can enter the cells; however, only $\text{ZnO}_{1-x}/\text{C}(0.6)$ shows multiple-wavelength excitability characteristic. It has been reported that carbon dots show excitation dependent photoluminescence behavior [52]. They are excitable at multiple wavelengths and emit light at different wavelengths. As shown in Fig. S13, the Zn-free C(0.6) sample possess very strong fluorescence emissions when excited at 488, 532, and 635 nm. This information lends to the credibility that $\text{ZnO}_{1-x}/\text{C}(0.6)$ have carbon dots on their surface, as also evidenced by HR-TEM images (Fig. 1).

To further explore the optical properties of the C(0.6) sample, PL measurements were performed by using different excitation wavelengths. As displayed in Fig. 5d, with excitation wavelengths at 350 and 400 nm, the PL spectra of C(0.6) sample show down-converted light emissions in the range of 400–600 nm, resulting from irradiative recombination of excitations at the surface of C(0.6). In addition to the strong down conversion PL property, the C(0.6) sample also exhibits a remarkable up-conversion behavior, which has been reported to be related to a two-photon absorption process [53]. The up-converted PL spectra of the C(0.6) sample with excitation wavelengths at 700, 750 and 800 nm (Fig. 5e) further verify its key role as a light harvester and converter, with the emission wavelength in the range of 410–560 nm. Hence, it is reasonable to suggest that the excellent photocatalytic response of $\text{ZnO}_{1-x}/\text{C}(0.6)$ in the NIR region arises from the up-converted emission energy of carbon dots to ZnO_{1-x} .

3.4.3. Electron transport properties

After the CO_2 adsorption and photogeneration of the charge carriers, their separation and transport are important parameters in the CO_2 reduction process [54]. Steady-state PL analyses were conducted to study the defects and the state of photogenerated charge carriers in the photocatalysts, with results depicted in Fig. 6a. The PL spectrum of ZnO exhibits a near-band-edge emission (NBE) at 388 nm (~ 3.2 eV), originating from the direct recombination of the free excitons [13]. However, the characteristic UV emission was not clearly distinguished in the $\text{ZnO}_{1-x}/\text{C}(0.6)$. It is noted that $\text{ZnO}_{1-x}/\text{C}(0.6)$ has additional three visible peaks at 460, 566 and 600 nm, respectively, which were ascribed to the neutral oxygen vacancy (V_o), singly charged oxygen vacancy (V_o^+) and doubly charged oxygen vacancy (V_o^{++}) [14]. The above findings indicate that a high concentration of oxygen defects was introduced into the $\text{ZnO}_{1-x}/\text{C}(0.6)$ sample. One should also mention that $\text{ZnO}_{1-x}/\text{C}(0.6)$ exhibits a weak emission at around 360 nm, which

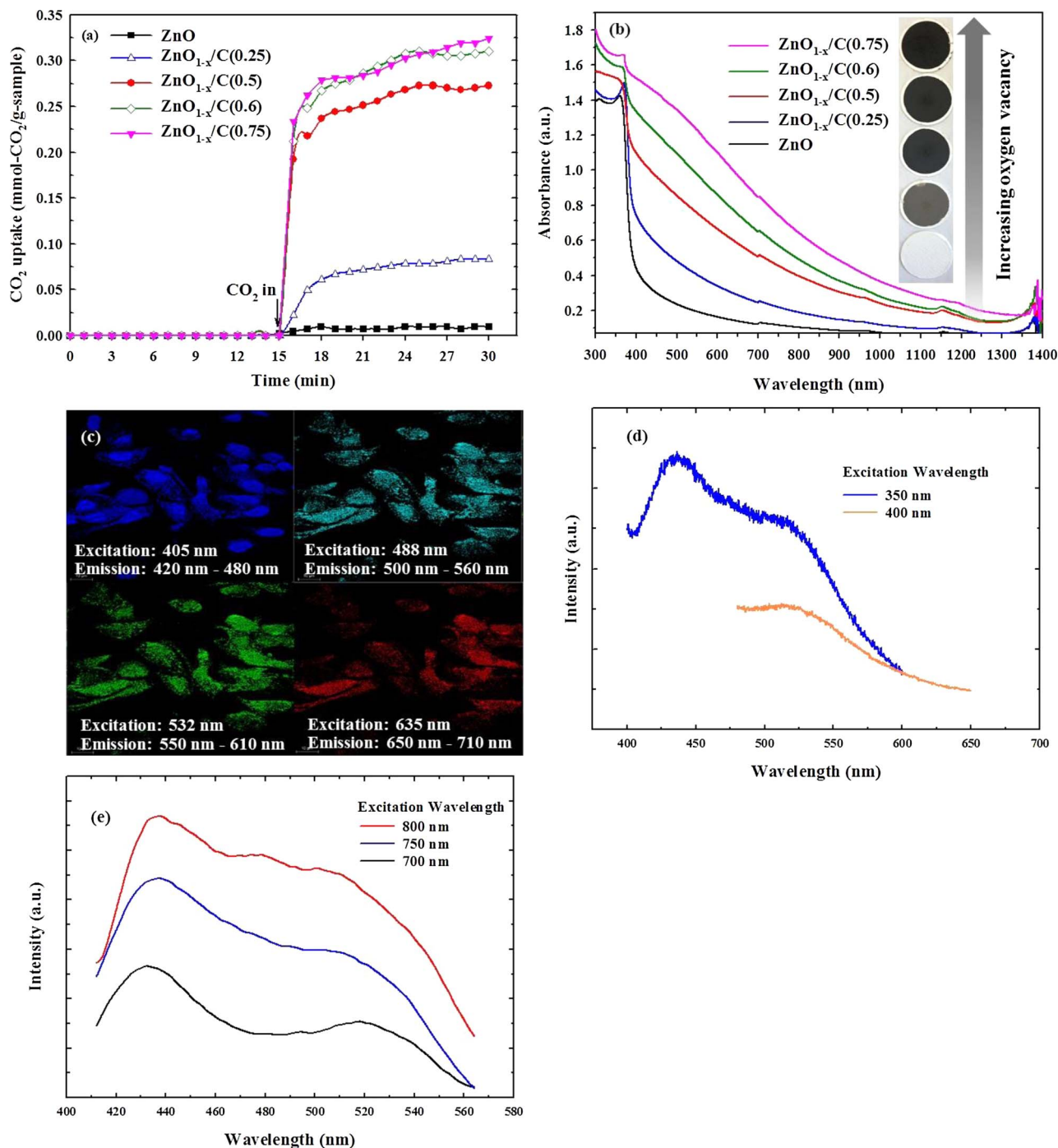


Fig. 5. (a) TGA isotherms for CO₂ adsorption, (b) Diffuse reflectance UV-vis spectra, (c) Confocal microscopy images of ZnO_{1-x}/C(0.6), (d) Down-converted PL spectra of the Zn-free C(0.6), and (e) Up-converted PL spectra of the Zn-free C(0.6). The legends indicate the excitation wavelength whereas the spectra show corresponding emission wavelengths.

is attributed to the emission from the C(0.6) carbon dots. As displayed in Fig. S14, C(0.6) carbon dots show a strong emission peak at around 360 nm (~3.5 eV), which is ascribed to the π - π^* transition of aromatic domains in the carbon dots [55].

The lifetime of charge carriers is an important parameter in the efficacy of the transfer and separation of photoexcited carriers in the photocatalytic system [34]. Hence, the lifetimes of the charge carriers of ZnO and ZnO_{1-x}/C(0.6) were measured by time-resolved PL (Fig. 6b). The carrier lifetime of ZnO_{1-x}/C(0.6) was estimated to be 8.25 ns, which was at least 27 times longer than that of ZnO, 0.307 ns (instrument response function is 0.2 ns), suggesting a drastically enhanced separation efficiency of photoexcited carriers on the ZnO_{1-x}/

C(0.6).

To support the above observation, the transient photocurrent responses of the samples were recorded with consecutive five switch-on/off cycles to understand the separation efficiency of the photogenerated charge carriers. As illustrated in Fig. 6c, all samples exhibit a steady photocurrent generation at each switch-on/off event, implying good stability. Additionally, the photocurrent response of ZnO disappears immediately right after the light is switched off, while a delayed decay of photocurrent is observed for ZnO_{1-x}/C(0.6). This observation may result from trapped charge carriers with extended lifetimes [56]. The above results suggest that the separation efficiency of the charge carriers was efficiently elevated and the recombination of electron-hole

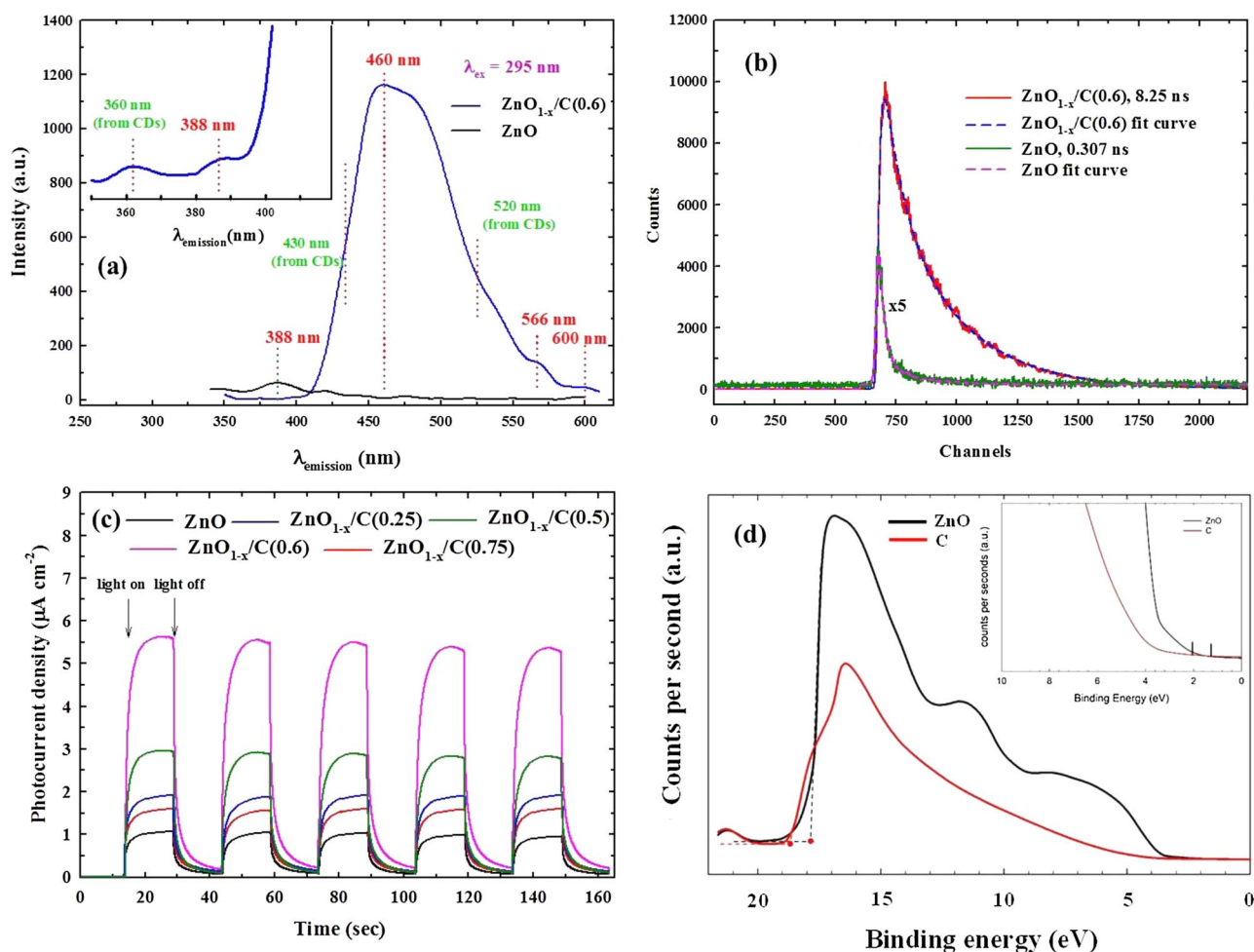


Fig. 6. (a) Steady-state PL measurements of the ZnO and $\text{ZnO}_{1-x}/\text{C}(0.6)$ under 295 nm excitation, (b) Time-resolved PL decay and its fitting curves (on the x axis, each channel is equivalent to 50 ps). (c) Time-dependent current density response for the ZnO and $\text{ZnO}_{1-x}/\text{C}$ samples under intermittent irradiation at a bias potential of 0.5 V vs. Ag/AgCl, and (d) UPS valence band spectra of ZnO and C extracted from $\text{ZnO}_{1-x}/\text{C}(0.6)$, and Inset of the figure represents the lower energy region of ZnO and C spectrum. The red dot corresponds to secondary electron edge, and black vertical tick mark represents the onset of the density of states.

pairs was greatly hindered.

We consider that this enhanced photocurrent response should be attributed to the efficient charge carrier transfer off-ered by oxygen vacancy defects, and to the superior conductivity contributed by the deposited carbons. Additionally, high concentration electron in the oxygen vacancy defect band can absorb photons and transit to the conduction band, leading to the improved photocurrent. One can see that the order of photocurrent responses among all the samples was perfectly consistent with the trend of photocatalytic CO_2 reduction activity, clearly demonstrating the significant positive impacts of the improved separation efficiency of charge carriers.

It was also noticed that $\text{ZnO}_{1-x}/\text{C}(0.75)$ had a relative lower photocurrent density than the other $\text{ZnO}_{1-x}/\text{C}$ samples. Although oxygen vacancy in the photocatalyst leads to formation of defect states within the bandgap, which strongly enhances the visible-light absorption [14,57]. An excessive number of oxygen vacancies remarkably increases the electron scattering, reducing the carrier mobility due to the formation of defect-related recombination centers, which rather prohibits the generation of photocurrent than to promote it [58]. On the other hand, there is an optimal load amount of carbon dots in the $\text{ZnO}_{1-x}/\text{C}$ composites as well. At first, the deposition of carbon dots tends to uniformly disperse on the surface and pores of ZnO_{1-x} , which can enhance utilization rate of UV-vis-NIR light. However, the carbon dots alone have no photoactivity for CO_2 reduction though they can absorb Vis-NIR light. Thus, we deduce that the photoreduction of CO_2 occurred on the ZnO_{1-x} surface. The higher amount of carbon dots

would result in a competition adsorption of CO_2 on the ZnO_{1-x} surface, which could lead to the decrease of photocatalytic capability for $\text{ZnO}_{1-x}/\text{C}(0.75)$ composites. Therefore, it is imperative to reasonably control the load amount of carbon dots on the ZnO_{1-x} .

Accordingly, one may conclude that although the enhanced adsorption of CO_2 may promote the photoreduction of CO_2 , the separation and transfer ability of photogenerated charge carriers seems to more significantly influence the photoactivity in these $\text{ZnO}_{1-x}/\text{C}$ samples.

Based on the above results, the difference in the photocatalytic activities of the $\text{ZnO}_{1-x}/\text{C}(0.6)$ samples prepared at different FuAR temperatures can also be well elucidated by the CO_2 -TGA and transient photocurrent response results (Fig. S15a and b). In this case, we believe that the low CO_2 adsorption abilities and fast recombination of electron-hole pairs are both responsible for the poor photocatalytic activities of $\text{ZnO}_{1-x}/\text{C}(0.6)$ -500 and $\text{ZnO}_{1-x}/\text{C}(0.6)$ -650. In brief, the physicochemical properties (surface area, optical property, and quantity of oxygen vacancies and deposited carbon) of the $\text{ZnO}_{1-x}/\text{C}$ composites can be easily tuned by altering the CA/Zn ratio and FuAR temperature, which in turn strongly influence both the CO_2 adsorption ability and separation efficiency of photogenerated charge carriers. Both parameters had cumulative effects on CO_2 photoreduction, which underlined the superior performance of $\text{ZnO}_{1-x}/\text{C}(0.6)$ for CO_2 photoreduction.

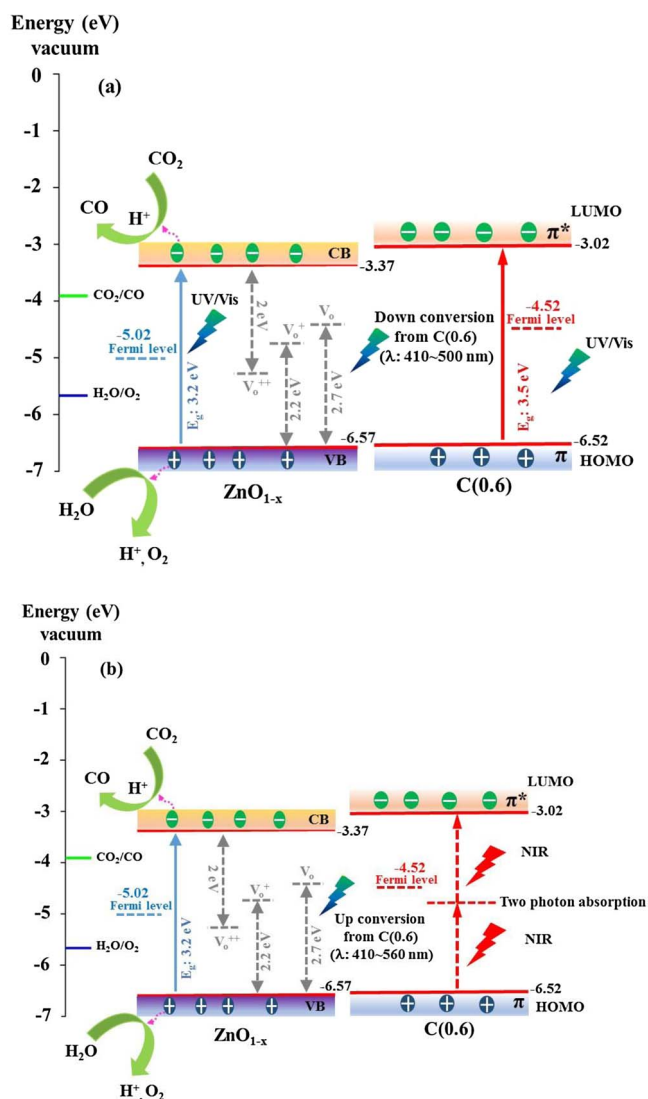


Fig. 7. Proposed mechanism for CO_2 photoreduction on $\text{ZnO}_{1-x}/\text{C}(0.6)$ under (a) UV/Vis light and (b) NIR only irradiation.

3.5. Mechanism of CO_2 photoreduction on $\text{ZnO}_{1-x}/\text{C}(0.6)$ under UV–vis–NIR irradiation

For an in-depth understanding of the mechanism, we determined the valence band (VB), conduction band (CB), and Fermi level of ZnO and C from the UPS spectrum (Fig. 6d). The long tail in the VB spectrum of C indicates five convoluted peaks corresponding to 2s σ , s-p hybridized state, 2p σ , 2p $\sigma + \pi$, and 2p π (from higher to lower energy). The various states in VB spectrum of C indicate the presence of bonding between carbon and oxygen, and carbon not being the pure elemental state [59]. The work function of the samples (energy of the Fermi level with respect to vacuum) is the difference between photon energy and the energy between the secondary electron emission edge (red circle mark) and the onset of the filled density of states (black vertical tick). The gap between the Fermi level and valence band maximum is the onset of the photoemission of valence electrons (black vertical tick), using which VB position is calculated [59]. CB minima are calculated using the VB maxima, Fermi level and the band gap determined from photoluminescence measurement.

On the basis of all the calculations, the energy level diagram along with the mechanisms for CO_2 photoreduction on $\text{ZnO}_{1-x}/\text{C}(0.6)$ under UV/visible and NIR light irradiation is proposed. As the $\text{ZnO}_{1-x}/\text{C}(0.6)$ is illuminated by UV/visible light (Fig. 7a), the ZnO_{1-x} is excited by

absorbing high energetic photons and produced electron-hole pairs. The introduction of surface oxygen vacancy (V_o , V_o^+ and V_o^{++}) defects has been reported to create donor energy band between the CB and VB of semiconductors [60]. Different from ZnO, which allows only direct excitation of electrons from the VB to the CB under UV light [13], the existence of oxygen vacancy defects in ZnO_{1-x} allows the indirect excitation of electrons from the sub-band to the CB by utilizing visible light. In this process, the V_o -induced defect sites act as springboards for the transition of electrons, so visible light can excite the electrons from the sub-band to the CB. On the other hand, since carbon dots alone showed no photoactivity for CO_2 reduction in our study, we deduce that the simultaneous reduction of CO_2 and oxidation of H_2O occurred on the ZnO_{1-x} surface, whereas the carbon dots function as light harvester and energy converter [61,62]. The carbon dot can absorb the high energetic photons in the UV light, followed by light emission located in the range of 400–500 nm (Fig. 5d), which further increase the light utilization of UV/visible light.

In the case of NIR light only (Fig. 7b), the carbon dots can absorb low energetic photons in the NIR, and then emit higher energy photons in the visible light region (410–560 nm) due to its up-converted fluorescence emissions (Fig. 5e), which in turn further excites ZnO_{1-x} to form electron-hole pairs. These photo-excited electrons and holes within the ZnO_{1-x} can either participate in photo-reactions at the surface or recombine. The recombination process has faster kinetics than the redox reactions and hence controls the efficiency of the photocatalytic process [63], which was also verified by our transient photocurrent response results. Furthermore, the hollow structure can enhance the light harvesting through multiple internal reflections, which can make better use of the light source and lead to improve the photocatalytic activity. Therefore, the overall photocatalytic activity of $\text{ZnO}_{1-x}/\text{C}(0.6)$ is enhanced during the process.

4. Conclusions

In summary, NIR-light-driven CO_2 reduction over a novel $\text{ZnO}_{1-x}/\text{carbon dots}$ composite was reported for the first time. The high NIR excitation of $\text{ZnO}_{1-x}/\text{carbon dots}$ can attribute to the presence of moderate amounts of oxygen vacancies and carbon dots. The $\text{ZnO}_{1-x}/\text{carbon dots}$ heterostructures synthesized through a fast, continuous and scalable FuAR approach possessed the enhanced UV, visible and NIR photocatalytic activity. This result is of significance in the utilization of a broad range of the solar spectrum, considerably broadening potential applications in sustainable energy sources and environmental cleanup. Future work will include the investigation of the control over shell thickness and particle size of hollow spheres to achieve high specific surface area, as well as possible tuning of the light absorption of the $\text{ZnO}_{1-x}/\text{carbon dots}$ to further enhance the CO_2 photoreduction efficiency.

Acknowledgments

Partial support from the National Science Foundation Grant CBET 1705864 and Department of Energy Grant DEFE0029161 are gratefully acknowledged. We appreciate the treasured guidance of Dr. Huafang Li, Washington University, the Institute of Materials Science and Engineering, for HR-TEM imaging and EDX elemental analysis.

Appendix A. Supplementary data

Supplementary material related to this article can be found, in the online version, at doi:<https://doi.org/10.1016/j.apcatb.2018.02.018>.

References

- [1] X. Chang, T. Wang, J. Gong, CO_2 photo-reduction: insights into CO_2 activation and reaction on surfaces of photocatalysts, *Energy Environ. Sci.* 9 (2016) 2177–2196.

- [2] J. Yu, J. Jin, B. Cheng, M. Jaroniec, A noble metal-free reduced graphene oxide–CdS nanorod composite for the enhanced visible-light photocatalytic reduction of CO₂ to solar fuel, *J. Mater. Chem. A* 2 (2014) 3407–3416.
- [3] W.-N. Wang, F. Wu, Y. Myung, D.M. Niedzwiedzki, H.S. Im, J. Park, P. Banerjee, P. Biswas, Surface engineered CuO nanowires with ZnO islands for CO₂ photo-reduction, *ACS Appl. Mater. Interfaces* 7 (2015) 5685–5692.
- [4] H.-Y. Wu, N.H. Nguyen, H. Bai, S. Chang, J.C.S. Wu, Photocatalytic reduction of CO₂ using molybdenum-doped titanate nanotubes in a MEA solution, *RSC Adv.* 5 (2015) 63142–63151.
- [5] L. Wang, Y. Wang, Y. Cheng, Z. Liu, Q. Guo, M.N. Ha, Z. Zhao, Hydrogen-treated mesoporous WO₃ as a reducing agent of CO₂ to fuels (CH₄ and CH₃OH) with enhanced photothermal catalytic performance, *J. Mater. Chem. A* 4 (2016) 5314–5322.
- [6] Y. Sang, H. Liu, A. Umar, Photocatalysis from UV/Vis to near-infrared light: towards full Solar-light spectrum activity, *ChemCatChem* 7 (2015) 559–573.
- [7] H.-Y. Wu, H. Bai, J.C.S. Wu, Photocatalytic reduction of CO₂ using Ti–MCM-41 photocatalysts in monoethanolamine solution for methane production, *Ind. Eng. Chem. Res.* 53 (2014) 11221–11227.
- [8] X. Ying Kong, Y. Yee Choo, S.-P. Chai, A. Kah Soh, A. Rahman Mohamed, Oxygen vacancy induced Bi₂WO₆ for the realization of photocatalytic CO₂ reduction over the full solar spectrum: from the UV to the NIR region, *Chem. Commun.* 52 (2016) 14242–14245.
- [9] X.Y. Kong, W.L. Tan, B.-J. Ng, S.-P. Chai, A.R. Mohamed, Harnessing Vis–NIR broad spectrum for photocatalytic CO₂ reduction over carbon quantum dots-decorated ultrathin Bi₂WO₆ nanosheets, *Nano Res.* (2017) 1–12.
- [10] K.M. Lee, C.W. Lai, K.S. Ngai, J.C. Juan, Recent developments of zinc oxide based photocatalyst in water treatment technology: a review, *Water Res.* 88 (2016) 428–448.
- [11] S. Girish Kumar, K.S.R. Koteswara Rao, Zinc oxide based photocatalysis: tailoring surface-bulk structure and related interfacial charge carrier dynamics for better environmental applications, *RSC Adv.* 5 (2015) 3306–3351.
- [12] L. Schmidt-Mende, J.L. MacManus-Driscoll, ZnO – nanostructures, defects, and devices, *Mater. Today* 10 (2007) 40–48.
- [13] J. Wang, Y. Xia, Y. Dong, R. Chen, L. Xiang, S. Komarneni, Defect-rich ZnO nanosheets of high surface area as an efficient visible-light photocatalyst, *Appl. Catal. B: Environ.* 192 (2016) 8–16.
- [14] Q. Zhu, C. Xie, H. Li, C. Yang, S. Zhang, D. Zeng, Selectively enhanced UV and NIR photoluminescence from a degenerate ZnO nanorod array film, *J. Mater. Chem. C* 2 (2014) 4566–4580.
- [15] X. Xin, T. Xu, J. Yin, L. Wang, C. Wang, Management on the location and concentration of Ti³⁺ in anatase TiO₂ for defects-induced visible-light photocatalysis, *Appl. Catal. B: Environ.* 176–177 (2015) 354–362.
- [16] L.-Y. Lin, Y. Nie, S. Kavadiya, T. Soundappan, P. Biswas, N-doped reduced graphene oxide promoted nano TiO₂ as a bifunctional adsorbent/photocatalyst for CO₂ photoreduction: effect of N species, *Chem. Eng. J.* 316 (2017) 449–460.
- [17] R. Miao, Z. Luo, W. Zhong, S.-Y. Chen, T. Jiang, B. Dutta, Y. Nasr, Y. Zhang, S.L. Suib, Mesoporous TiO₂ modified with carbon quantum dots as a high-performance visible light photocatalyst, *Appl. Catal. B: Environ.* 189 (2016) 26–38.
- [18] H. Li, X. He, Z. Kang, H. Huang, Y. Liu, J. Liu, S. Lian, C.H.A. Tsang, X. Yang, S.-T. Lee, Water-soluble fluorescent carbon quantum dots and photocatalyst design, *Angew. Chem. Int. Ed.* 49 (2010) 4430–4434.
- [19] Z. Ma, H. Ming, H. Huang, Y. Liu, Z. Kang, One-step ultrasonic synthesis of fluorescent N-doped carbon dots from glucose and their visible-light sensitive photocatalytic ability, *New J. Chem.* 36 (2012) 861–864.
- [20] H. Bozetine, Q. Wang, A. Barras, M. Li, T. Hadjersi, S. Szunerits, R. Boukherroub, Green chemistry approach for the synthesis of ZnO–carbon dots nanocomposites with good photocatalytic properties under visible light, *J. Colloid Interface Sci.* 465 (2016) 286–294.
- [21] J. Wang, Y. Li, J. Ge, B.-P. Zhang, W. Wan, Improving photocatalytic performance of ZnO via synergistic effects of Ag nanoparticles and graphene quantum dots, *Phys. Chem. Chem. Phys.* 17 (2015) 18645–18652.
- [22] X.-Y. Zhang, J.-K. Liu, J.-D. Wang, X.-H. Yang, Mass Production, Enhanced visible light photocatalytic efficiency, and application of modified ZnO nanocrystals by carbon dots, *Ind. Eng. Chem. Res.* 54 (2015) 1766–1772.
- [23] Y. Li, B.-P. Zhang, J.-X. Zhao, Z.-H. Ge, X.-K. Zhao, L. Zou, ZnO/carbon quantum dots heterostructure with enhanced photocatalytic properties, *Appl. Surf. Sci.* 279 (2013) 367–373.
- [24] H. Yu, H. Zhang, H. Huang, Y. Liu, H. Li, H. Ming, Z. Kang, ZnO/carbon quantum dots nanocomposites: one-step fabrication and superior photocatalytic ability for toxic gas degradation under visible light at room temperature, *New J. Chem.* 36 (2012) 1031–1035.
- [25] K. Okuyama, I. Wuled Lenggoro, Preparation of nanoparticles via spray route, *Chem. Eng. Sci.* 58 (2003) 537–547.
- [26] G.L. Messing, S.-C. Zhang, G.V. Jayanthi, Ceramic powder synthesis by spray pyrolysis, *J. Am. Ceram. Soc.* 76 (1993) 2707–2726.
- [27] Y. Zhu, S.H. Choi, X. Fan, J. Shin, Z. Ma, M.R. Zachariah, J.W. Choi, C. Wang, Recent progress on spray pyrolysis for high performance electrode materials in lithium and sodium rechargeable batteries, *Adv. Energy Mater.* 7 (2017) 1601578–1601619.
- [28] G. Jian, L. Liu, M.R. Zachariah, Facile aerosol route to hollow CuO spheres and its superior performance as an oxidizer in nanoenergetic gas generators, *Adv. Funct. Mater.* 23 (2013) 1341–1346.
- [29] Y. Jiang, S. Yang, Z. Hua, H. Huang, Sol–Gel autocombustion synthesis of metals and metal alloys, *Angew. Chem. Int. Ed.* 48 (2009) 8529–8531.
- [30] X. Yu, B. Kim, Y.K. Kim, Highly enhanced photoactivity of anatase TiO₂ nanocrystals by controlled hydrogenation-induced surface defects, *ACS Catal.* 3 (2013) 2479–2486.
- [31] A. Sinhamahapatra, J.-P. Jeon, J.-S. Yu, A new approach to prepare highly active and stable black titania for visible light-assisted hydrogen production, *Energy Environ. Sci.* 8 (2015) 3539–3544.
- [32] Z. Wang, C. Yang, T. Lin, H. Yin, P. Chen, D. Wan, F. Xu, F. Huang, J. Lin, X. Xie, M. Jiang, Visible-light photocatalytic, solar thermal and photoelectrochemical properties of aluminium-reduced black titania, *Energy Environ. Sci.* 6 (2013) 3007–3014.
- [33] S. Mukhopadhyay, P.P. Das, S. Maity, P. Ghosh, P.S. Devi, Solution grown ZnO rods: synthesis, characterization and defect mediated photocatalytic activity, *Appl. Catal. B: Environ.* 165 (2015) 128–138.
- [34] J. Wang, Y. Xia, H. Zhao, G. Wang, L. Xiang, J. Xu, S. Komarneni, Oxygen defects-mediated Z-scheme charge separation in g-C₃N₄/ZnO photocatalysts for enhanced visible-light degradation of 4-chlorophenol and hydrogen evolution, *Appl. Catal. B: Environ.* 206 (2017) 406–416.
- [35] S. Lu, S. Guo, P. Xu, X. Li, Y. Zhao, W. Gu, M. Xue, Hydrothermal synthesis of nitrogen-doped carbon dots with real-time live-cell imaging and blood–brain barrier penetration capabilities, *Int. J. Nanomed.* 11 (2016) 6325–6336.
- [36] C.A. Aggelopoulos, M. Dimitropoulos, A. Govatsi, L. Sygellou, C.D. Tsakiroglou, S.N. Yannopoulos, Influence of the surface-to-bulk defects ratio of ZnO and TiO₂ on their UV-mediated photocatalytic activity, *Appl. Catal. B: Environ.* 205 (2017) 292–301.
- [37] L.-W. Zhang, H.-B. Fu, Y.-F. Zhu, Efficient TiO₂ photocatalysts from surface hybridization of TiO₂ particles with graphite-like carbon, *Adv. Funct. Mater.* 18 (2008) 2180–2189.
- [38] F. Pan, J. Jin, X. Fu, Q. Liu, J. Zhang, Advanced oxygen reduction electrocatalyst based on nitrogen-doped graphene derived from edible sugar and urea, *ACS Appl. Mater. Interfaces* 5 (2013) 11108–11114.
- [39] L. Yu, G. Li, X. Zhang, X. Ba, G. Shi, Y. Li, P.K. Wong, J.C. Yu, Y. Yu, Enhanced activity and stability of carbon-decorated cuprous oxide mesoporous nanorods for CO₂ reduction in artificial photosynthesis, *ACS Catal.* 6 (2016) 6444–6454.
- [40] W. Stählin, H.R. Oswald, The infrared spectrum and thermal analysis of zinc hydroxide nitrate, *J. Solid State Chem.* 3 (1971) 252–255.
- [41] W. Wang, D. Xu, B. Cheng, J. Yu, C. Jiang, Hybrid carbon@TiO₂ hollow spheres with enhanced photocatalytic CO₂ reduction activity, *J. Mater. Chem. A* 5 (2017) 5020–5029.
- [42] Y. Nie, W.-N. Wang, Y. Jiang, J. Fortner, P. Biswas, Crumpled reduced graphene oxide–amine–titanium dioxide nanocomposites for simultaneous carbon dioxide adsorption and photoreduction, *Catal. Sci. Technol.* 6 (2016) 6187–6196.
- [43] X. He, Z. Gan, S. Fisenko, D. Wang, H.M. El-Kaderi, W.-N. Wang, Rapid formation of metal–organic frameworks (MOFs) based nanocomposites in microdroplets and their applications for CO₂ photoreduction, *ACS Appl. Mater. Interfaces* 9 (2017) 9688–9698.
- [44] S. Kumar, M.A. Isaacs, R. Trofimovaite, L. Durndell, C.M.A. Parlett, R.E. Douthwaite, B. Coulson, M.C.R. Cockett, K. Wilson, A.F. Lee, P25@CoAl layered double hydroxide heterojunction nanocomposites for CO₂ photocatalytic reduction, *Appl. Catal. B: Environ.* 209 (2017) 394–404.
- [45] W.-N. Wang, J. Park, P. Biswas, Rapid synthesis of nanostructured Cu–TiO₂–SiO₂ composites for CO₂ photoreduction by evaporation driven self-assembly, *Catal. Sci. Technol.* 1 (2011) 593–600.
- [46] S. Xie, Y. Wang, Q. Zhang, W. Fan, W. Deng, Y. Wang, Photocatalytic reduction of CO₂ with H₂O: significant enhancement of the activity of Pt–TiO₂ in CH₄ formation by addition of MgO, *Chem. Commun.* 49 (2013) 2451–2453.
- [47] S. Azad, M.H. Engelhard, L.-Q. Wang, Adsorption and reaction of CO and CO₂ on oxidized and reduced SrTiO₃(100) surfaces, *J. Phys. Chem. B* 109 (2005) 10327–10331.
- [48] K. Xie, N. Umezawa, N. Zhang, P. Reunchan, Y. Zhang, J. Ye, Self-doped SrTiO₃–s photocatalyst with enhanced activity for artificial photosynthesis under visible light, *Energy Environ. Sci.* 4 (2011) 4211–4219.
- [49] Y. Zheng, C. Chen, Y. Zhan, X. Lin, Q. Zheng, K. Wei, J. Zhu, Y. Zhu, Luminescence and photocatalytic activity of ZnO nanocrystals: correlation between structure and property, *Inorg. Chem.* 46 (2007) 6675–6682.
- [50] T. Xia, P. Wallenmeyer, A. Anderson, J. Murowchick, L. Liu, X. Chen, Hydrogenated black ZnO nanoparticles with enhanced photocatalytic performance, *RSC Adv.* 4 (2014) 41654–41658.
- [51] L. Cao, S. Sahu, P. Anilkumar, C.E. Bunker, J. Xu, K.A.S. Fernando, P. Wang, E.A. Gulians, K.N. Tackett, Y.-P. Sun, Carbon nanoparticles as visible-light photocatalysts for efficient CO₂ conversion and beyond, *J. Am. Chem. Soc.* 133 (2011) 4754–4757.
- [52] H. Wang, C. Sun, X. Chen, Y. Zhang, V.L. Colvin, Q. Rice, J. Seo, S. Feng, S. Wang, W.W. Yu, Excitation wavelength independent visible color emission of carbon dots, *Nanoscale* 9 (2017) 1909–1915.
- [53] R. Miao, Z. Luo, W. Zhong, S.-Y. Chen, T. Jiang, B. Dutta, Y. Nasr, Y. Zhang, S.L. Suib, Mesoporous TiO₂ modified with carbon quantum dots as a high-performance visible light photocatalyst, *Appl. Catal. B: Environ.* 189 (2016) 26–38.
- [54] J. Huo, Y. Hu, H. Jiang, C. Li, In situ surface hydrogenation synthesis of Ti³⁺ self-doped TiO₂ with enhanced visible light photoactivity, *Nanoscale* 6 (2014) 9078–9084.
- [55] J. Ke, X. Li, Q. Zhao, B. Liu, S. Liu, S. Wang, Upconversion carbon quantum dots as visible light responsive component for efficient enhancement of photocatalytic performance, *J. Colloid Interface Sci.* 496 (2017) 425–433.
- [56] L. Chen, D. Meng, X. Wu, A. Wang, J. Wang, Y. Wang, M. Yu, In situ synthesis of V⁴⁺ and Ce³⁺ self-doped BiVO₄/CeO₂ heterostructured nanocomposites with high surface areas and enhanced visible-light photocatalytic activity, *J. Phys. Chem. C* 120 (2016) 18548–18559.
- [57] A. Abdolhazadeh Ziabari, S.M. Rozati, Carrier transport and bandgap shift in n-type

- degenerate ZnO thin films: the effect of band edge nonparabolicity, *Phys. B: Condens. Matter* 407 (2012) 4512–4517.
- [58] H. Tan, Z. Zhao, M. Niu, C. Mao, D. Cao, D. Cheng, P. Feng, Z. Sun, A facile and versatile method for preparation of colored TiO₂ with enhanced solar-driven photocatalytic activity, *Nanoscale* 6 (2014) 10216–10223.
- [59] G. Singh, V.D. Botcha, D.S. Sutar, S.S. Talwar, R.S. Srinivasa, S.S. Major, Graphite mediated reduction of graphene oxide monolayer sheets, *Carbon* 95 (2015) 843–851.
- [60] J. Hou, H. Cheng, C. Yang, O. Takeda, H. Zhu, Hierarchical carbon quantum dots/hydrogenated- γ -TaON heterojunctions for broad spectrum photocatalytic performance, *Nano Energy* 18 (2015) 143–153.
- [61] H. Yu, R. Shi, Y. Zhao, G.I.N. Waterhouse, L.-Z. Wu, C.-H. Tung, T. Zhang, Smart utilization of carbon Dots in semiconductor photocatalysis, *Adv. Mater.* 28 (2016) 9454–9477.
- [62] J. Hou, S. Cao, Y. Wu, F. Liang, L. Ye, Z. Lin, L. Sun, Perovskite-based nanocubes with simultaneously improved visible-light absorption and charge separation enabling efficient photocatalytic CO₂ reduction, *Nano Energy* 30 (2016) 59–68.
- [63] J. Wen, X. Li, W. Liu, Y. Fang, J. Xie, Y. Xu, Photocatalysis fundamentals and surface modification of TiO₂ nanomaterials, *Chin. J. Catal.* 36 (2015) 2049–2070.